JOTCSA Journal of the Turkish Chemical Society Section: A Chemistry

TURKISH CHEMICAL SOCIETY

Adsorption of an Anthracycline Drug on Glass Powder: Kinetics, Equilibria, and Thermodynamics Adsorption of Anthracycline Drug on Glass Powder: Kinetics, Equilibria and Thermodynamics

Ayşe Engin Kurtoğlu[1*], Remziye Yeşim Cantürk Talman[2]

[1]Istanbul University-Cerrahpaşa, Faculty of Engineering, Department of Chemistry, Istanbul, Türkiye.
[2]Marmara University, Faculty of Pharmacy, Professional Pharmaceutical Sciences, Department of Pharmaceutical Chemistry, Istanbul, Türkiye.

Abstract: Glass powder was treated with concentrated sulfuric acid and boiled several times to prepare a novel porous adsorbent for drug adsorption. Mitoxantrone was selected as a probe molecule for anthracycline group anticancer drugs. Kinetic studies using two different particle radii of $r < 125$ and $125 < r < 250$ μm in 0.02 and 0.10 mM Mitoxantrone solutions showed that both the rate constants and the diffusion coefficient decreased with increasing particle size. The data were applied to the pseudo-first order, two-first order and homogeneous surface diffusion models. According to the two-first-order model, an initial fast surface reaction is followed by the slow diffusion of drug molecules into the pores of acid-treated glass powder making this material a potential candidate as a drug carrier. On the other hand, ultra-fast adsorption of Mitoxantrone on the untreated glass surface indicates that chemisorption dominates the drug adsorption process. They can be used as environmentally friendly adsorbents for water treatment. The proposed mechanisms are also consistent with the thermodynamic results obtained from temperature dependence of adsorption in the 298–350 K range. Mitoxantrone adsorption on non-treated glass powder is exothermic in nature whereas the driving force of the endothermic process on acid-treated glass powder is the positive entropy change. L–S-shaped adsorption isotherms were obtained in the 0.012 – 1.200 mmol/L initial concentration range. The combined Langmuir–Liu model fits better to the isotherms than the conventional two-step model.

Keywords: Anthracycline drug, Mitoxantrone, Glass powder, Acid treatment, Adsorption.

Submitted: March 30, 2026. **Accepted:** June 1, 2026.

Cite this: Kurtoğlu AE, Cantürk Talman RY. Adsorption of an Anthracycline Drug on Glass Powder: Kinetics, Equilibria, and Thermodynamics Adsorption of Anthracycline Drug on Glass Powder: Kinetics, Equilibria and Thermodynamics. JOTCSA. 2026, **1919335**, 1-13.

DOI: https://doi.org/10.18596/jotcsa.1919335

Izlik page: https://izlik.org/JA89SK53PS

***Corresponding author's E-mails:** kurtoglu@iuc.edu.tr

1. INTRODUCTION

Mitoxantrone (Mx) is an anticancer drug structurally belonging to anthracyclines, which are used in up to 75% chemotherapeutic treatments (1). Numerous mesoporous adsorbents have been synthesized to assist drug loading and controlled release. It has been shown that Mx is reversibly adsorbed on superparamagnetic iron oxide nanoparticles (NPs) (2-4) and mesoporous SiO_2 NPs (5-6), which are potential drug carriers.

Zr-based metal organic frameworks (MOFs) UiO-62 and UiO-62-NH_2 have been examined as drug carriers for Mx (7). Modification with $-NH_2$ to reduce cytotoxicity of UiO-62 decreases the loading capacity from 371 to 208 mg/g. Similarly, Mx adsorption on magnetic single-walled carbon nanotubes (mSWCNT) decreases from 268 mg/g to 145 mg/g when coated with bovine serum albumin (8). Multiwalled carbon nanotubes (MWCNT) have a somewhat lower capacity (200 mg/g) than that of mSWCNT (9). Biosynthesized manganese nanoparticles (MNPs) adsorb 97.4 mg/g Mx (10).

Biocompatible mesoporous bioactive glasses (MBGs) composed of varying ratios of $SiO_2/Na_2O/CaO/P_2O_5$ are desirable and versatile materials in healthcare. Biocompatible glass microspheres with diameters in the micrometer range have also attracted great attention from researchers for biomedical applications as microcontainers for drug delivery (11-13). The MBGs are extensively used as drug-delivery carrier. Chemical compositions and textural properties of MBGs including surface area and pore properties depend on the synthesis method (14-16). Loading efficiency also varies with molecular size and structure of drugs. In recent studies conducted with levofloxacin (17,18), ciprofloxacin (18, 19), ibuprofen (20), ropivacaine (21), fluorouracil (22), simvastatin (23), cisplatin (24) and amoxicillin (18,25) on different bioglass carriers have shown that drug-loading efficiency varies over a wide range of 0.25–90% (14,15).

Mesoporous glass powder has also been prepared from commercial glass and by leaching with both organic and mineral acids (26). Acid leaching of all types of glasses including lead-silicate, boro-silicate and soda-lime-silicate glass follows the same route. A silica-rich gel phase is formed on the particle surface due to the exchange of alkali and alkaline-earth ions with protons of the leaching acid. This leads to formation of porous structures on the stabilized silica layer depending on the leaching time, the type of acid used, and the temperature (27-31).

Drug adsorption studies have also been conducted for environmental remediation. Solid waste materials such as sugarcane bagasse as sugarcane bagasse (32), acidified red mud (33), fly ash and acid treated fly ash (34) are frequently used as low cost adsorbents for drug removal from aquatic media. Huge amounts of glass waste are discharged every day to the environment. They can also be considered as costless and eco-friendly adsorbent for drug removal as well as potential drug carrier.

In this purpose, Mx adsorption on acid treated glass powder (ATGP) was compared with the GP at two different particle radius of $r < 125$ μm and $125 < r < 250$ μm. Results of adsorption kinetics, equilibria and thermodynamics revealed that GP is more convenient for environmental cleaning while ATGP has a potential as a drug carrier.

2. MATERIALS AND METHODS

2.1. Chemicals

Mitoxantrone dihydrochloride (Mx), 1,4-dihydroxy-5,8-bis{[2-[(2-hydroxyethyl)amino]-ethyl] amino]-9,10-anthracenedione; 1,4-dihydroxy-5,8-bis[2-(2-hydroxyethylamino) ethylamino]-anthracene-9,10-dione used as model molecule for anticancer drugs belonging to anthracyclines (Mw = 517.7 g/mol) (Figure 1). 3D chemical structure of the mitoxantrone designed using "Avogadro" molecular modeling software program with Open Babel version of 2.3.2. It was supplied by Sigma-Aldrich ≥ 97% CAS Number 70476-82-3. Molecular dimensions of Mx were calculated as 19.4 × 12.3 $Å^2$.

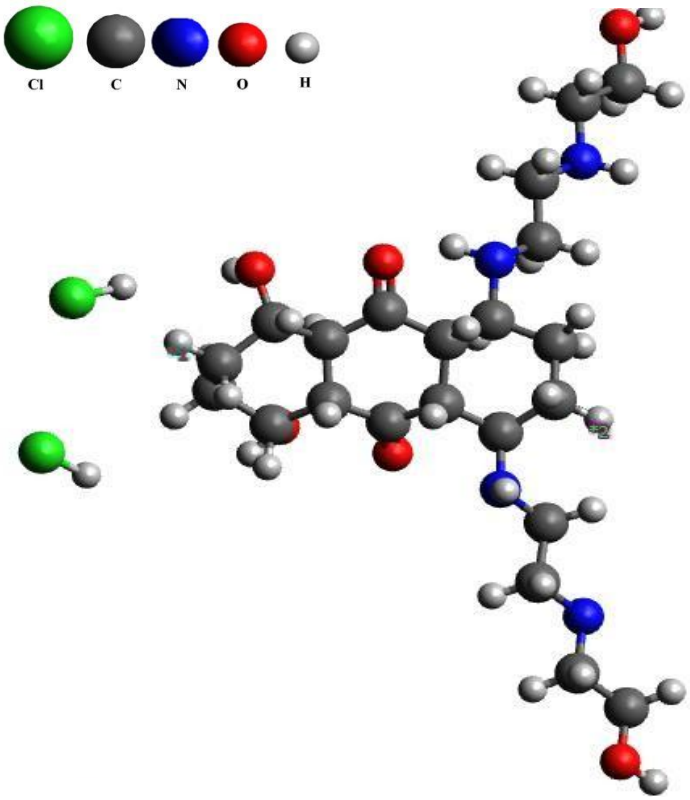

Figure 1: Chemical composition of Mitoxantrone dihydrochloride (Mx).

Concentration of aqueous Mx solution was determined from the UV-spectrum recorded with Perkin Elmer 554 spectrometer by measuring the absorbance of the peak at λ_{max} 606 nm. It changes linearly in 0.4×10^{-5} - 10×10^{-5} mol/L range (r^2= 0.999).

2.2. Preparation and Characterization of Acid Treated Glass (ATGP) Powder

Chemical composition of the glass powder is as follows by weight: SiO_2, 72.5%; Al_2O_3, 1.2%; Fe_2O_3, 0.37%; TiO_2, 0.173%; CaO, 7.82%; MgO, 3.96%; Na_2O, 13.64%; and K_2O, 0.26% (35,36).

60 g of the GP was contacted with 100 mL of sulfuric acid (98 %) for five days in an oven at 298 K. After it was filtered and washed several times it was boiled for 1 hour in 300 mL distilled water. Its conductivity and pH were measured after cooling to room temperature. This procedure was repeated for nine times until obtaining constant conductivity and pH. After separation from solution the GP was dried at 383 K for 1 day. The GP was sieved r < 125 and 125 < r < 250 μm and stored in desiccator until using adsorption experiments.

The Ultraviolet Visible Near Infrared Reflectance (UV-VIS-NIR) spectra of the GP and ATGP were recorded using an UV-VIS-NIR (Cary 500, Varian) spectrometer with a diffuse reflectance accessory (DRA-CA-50D).

Pore properties of the ATGP were evaluated from nitrogen adsorption-desorption experiments conducted at 77.4 K using a Quantachrome Autosorb Automated Gas Sorption System. Specific surface area (S_{BET}) was evaluated from adsorption isotherm using Brauner-Emmet-Teller (BET) theory. The pore size distribution was calculated on the basis of desorption isotherms by using the Barrett-Joyner-Halenda (BJH) method. All calculations were made by employing a computer program Autosorb for Windows version 1.19.

2.3. Adsorption Experiments

In order to determine the equilibrium time of 0.25 g adsorbents were contacted with 25 mL Mx solution of 0.02 and 0.10 mmol/L initial concentration. The GP was attained to equilibrium in seconds therefore its time dependent adsorption couldn't be determined. The concentration change of Mx was followed for 5 days in varying time intervals until equilibrium is established for ATGP under static conditions at 298 K.

Adsorption equilibria for r < 125 μm size GP and ATGP were investigated at different initial concentration of Mx solutions in 0.012 – 1.165 mmol/L range until 5 days while 125 < r < 250 μm size adsorbents were contacted with 0.030 – 1.200 mmol/L solutions.

Each experiment was made in triplicate. Average value of adsorbed quantity was used in kinetics and isotherm plots. Deviation was less than 5 %. It was indicated with error bars.

The conductivity and pH of the initial and final Mx solutions were measured using Metrohm Conductometer E 365 B and Metrohm pH/mV Electrometer 265. Effect of temperature on adsorption equilibria was also studied in 0.1 mM Mx solution in 298 – 350 K range.

3. RESULTS AND DISCUSSIONS

3.1. Structural and Textural Properties

UV-VIS-NIR spectroscopy can provide information about both crystalline and amorphous structures (37,38). UV-VIS-NIR spectra of the GP and ATGP are shown in Figure 2. More intense peaks belonging to SiO_2 are observed on the ATGP spectrum comparing to GP. This arises from enrichment of silica phase on the surface due to exchanging of alkali and alkali earth cations with hydroxonium ions during acid treatment (30). The peak at 844 nm is also superimposed by increasing content of amorphous Fe_2O_3 in $Al_2O_3nSiO_2$ phase on the surface layer (39). The peak at 1984 nm is also well matched with ferric species (37,40,41).

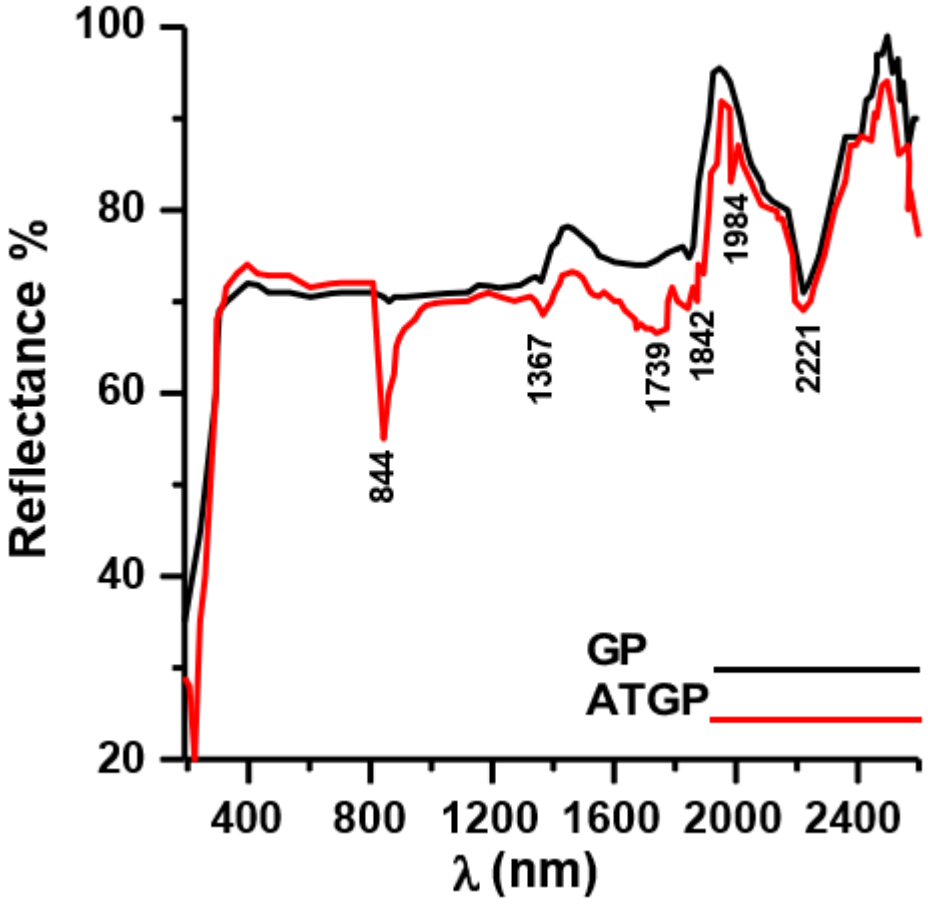

Figure 2: Comparison of UV-VIS-NIR spectra of GP and ATGP.

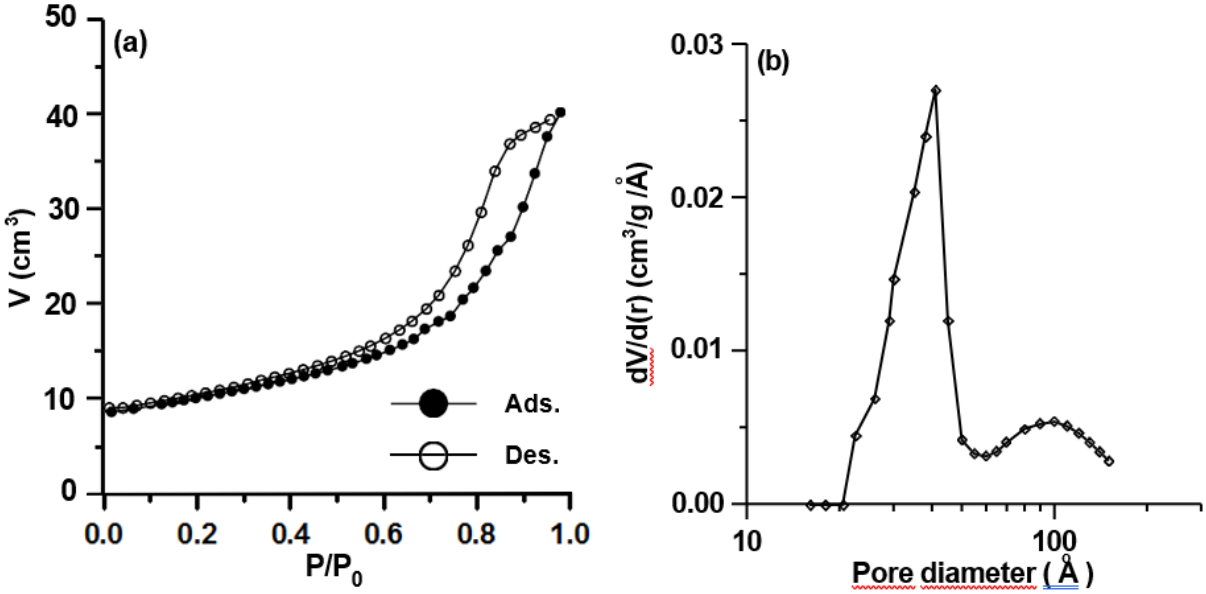

Figure 3: a) Nitrogen adsorption-desorption isotherm and b) pore size distribution of ATGP.

The BET surface was calculated as 6.5 m^2/g from the linear segment of the N_2 adsorption isotherm in average relative pressure range 0.04-0.30 using multi-point BET method (Figure 3a). Mean pore diameter was estimated as ~ 40 Å from the pore size distribution (PSD) plot in mesoporous range of 20 – 180 Å (Figure 3b).

3.2. Adsorption Kinetics of Mx on the ATGP

Adsorbed quantity of Mx at varying time was determined from the following equation:

$$q_t = C_0 F_t \frac{V}{m_a} \quad (1)$$

where C_0 is the initial concentration of M_x, F_t is the adsorbed fraction at time t, V is the solution volume and m_a is the adsorbent mass. Time dependency of adsorption on the ATGP followed until five days in 0.02 and 0.10 mM Mx solutions is depicted in Figures 4a and b, respectively.

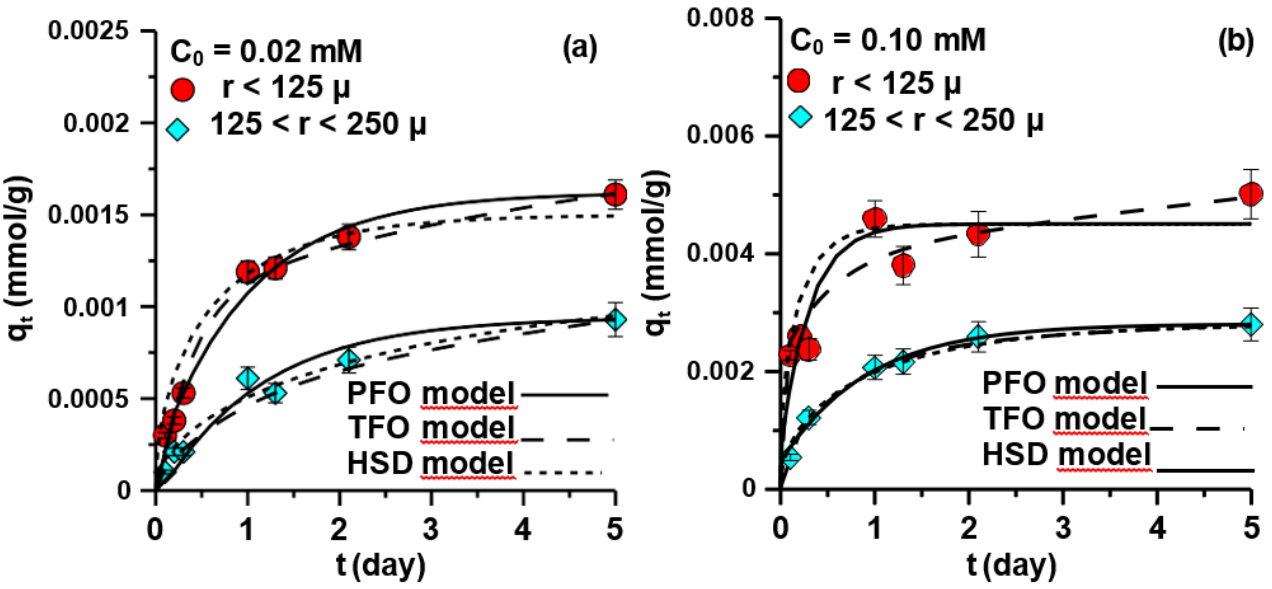

Figure 4: Particle size dependency of adsorption kinetics of Mx on ATGP at different initial concentrations: a) C_0= 0.02 mM and b) C_0= 0.10 mM.

Adsorbed amount of Mx decreased with increasing particle size. The time dependent results were fit to the pseudo-first order (PFO) and two-first order (TFO) and homogeneous surface diffusion (HSD) models.

The PFO model is applied using the Lagergren's rate expression described as (42):

$$q_t = q_e(1 - e^{-k_1 t}) \quad (2)$$

Here, k_1 is the rate constant and q_e is the adsorbed quantity at equilibrium.

The HSD model assumes diffusion of sorbate in one direction on a solid surface. Vermeulen's approximation presented below provides a simple solution for estimation of the diffusion coefficient (43).

$$q_t = q_e \left[1 - exp\left(-\pi^2 \frac{D_s t}{r^2}\right)\right]^{0.5} \quad (3)$$

where D_s is the solid phase surface diffusion coefficient and r is the average particle radius.

According to two-first order model adsorbate molecules are adsorbent with different mechanisms on different adsorption sites. The fast surface reaction is followed by slow diffusion process. Adsorbed fraction at any time can be written as follows based on radioactive decay law for radionuclide mixtures with different half-life (44).

$$F_t = 1 - \left[F_{t,\infty} e^{-k_f t} + \left(1 - F_{t,\infty}\right) e^{-k_s t}\right] \quad (4)$$

Here $F_{t,\infty}$ is adsorbed fraction at infinite time, k_f and k_s are the first order rate constants of the initial fast and the following slow adsorption processes.

The model parameters were estimated by minimizing the standard deviation (σ) between experimental and theoretical q_t values:

$$\sigma = \left[\frac{1}{n_e}\sum_{i=1}^{n}\left(q_{t,exp} - q_{t,cal}\right)^2\right]^{0.5} \quad (5)$$

where n_e is the number of experimental observations.

The theoretical curves presented in Figures 4a and b were estimated using the model parameters given in Table 1.

Adsorbed quantity q_e increased from 1.62 to 5.10 mmol/g as Mx concentration increased from 0.02 to 0.10 mmol/g according to PSO model. They were found to be 1.50 and 4.50 mmol/g, respectively, based on HSD model.

Table 1: The kinetic model parameters for the Mx adsorption on the ATGP with different particle radius in 0.02 and 0.10 mM Mx solutions.

Model	C_0 mmol/L	r μm	q_e ×10³ mmol/g	k_1 ×10⁵ s⁻¹		σ ×10³ mmol/g
PFO	0.02	r < 125	1.62	1.14		0.05
		125 < r < 250	0.94	1.02		0.07
	0.10	r < 125	5.10	3.82		0.47
		125 < r < 250	2.80	1.27		0.08
			$F_{t,\infty}$	k_f ×10⁵ s⁻¹	k_s ×10⁷ s⁻¹	
TFO	0.02	r < 125	0.5165	3.25	21.30	0.06
		125 < r < 250	0.2614	1.25	7.46	0.06
	0.10	r < 125	0.3935	2.15	4.26	0.38
		125 < r < 250	0.2424	1.62	1.15	0.08
			q_e ×10³ mmol/g	D_s × 10¹⁴ m²/s		
HSD	0.02	r < 125	1.50	1.79		0.14
		125 < r < 250	1.20	1.45		0.05
	0.10	r < 125	4.50	6.33		0.62
		125 < r < 250	2.80	5.06		0.39

Results reveal that both rate constants and surface diffusion coefficients decrease with increasing particle size. The magnitude of the $D_s \sim 10^{-14}$ m²/s indicates that pore diffusion is the rate limiting step in Mx adsorption on the ATGP. On the other hand, ultrafast Mx adsorption on the GP completed in seconds is also an indication of chemisorption of Mx on the surface. The k_f values for the fast initial process are nearly 10^2 times higher than the k_s values of the slow process on the ATGP. The first fast and the following slow processes can be attributed to fast surface reactions and the slower pore diffusion, respectively. It has been reported that Mx adsorption on the porous carbon follows similar routes and it releases nearly the same rate in saline-phosphate buffer at pH 7.40 which equals to blood pH (45). The TFO results for porous ATGP reveal that it is a promising drug carrier for Mx and its analogues.

3.3. Adsorption Equilibria of Mx on the GP and ATGP

Adsorption isotherms of Mx on the GP and ATGP with r < 125 and 125 < r < 0.125 μm size are presented in Figures 5a and b respectively. Their pH and conductivity values before and after adsorption are also shown in Figures 5 (a', b') and 5 (a'', b''), respectively.

Two-step adsorption isotherms are observed for both GP and ATGP. This type of isotherms is typical in surfactant adsorption (46,47) which described with the following general isotherm formula (46):

$$q_e = \frac{max K_1 C_e \left(\frac{1}{n} + K_2 C_e^{n-1}\right)}{K_1 C_e \left(1 + K_2 C_e^{n-1}\right)} \quad (6)$$

Here, q_{max} is the adsorption capacity corresponding to the second plateau of the two-step curve, n is the aggregation number; C_e is the equilibrium concentration; K_1 and K_2 are the constants proportional to hemi-micelle and micelle capacity of surfactant, respectively.

It transforms to following equation for L-S shaped isotherm for $K_1 C_e >> 1$

$$q_e = \frac{max \left(\frac{1}{n} + K_2 C_e^{n-1}\right)}{\left(1 + K_2 C_e^{n-1}\right)} \quad (7)$$

Isotherm curves calculated using Eq. 7 quite deviate from the experimental points.

The data also were modeled based on the following combined Langmuir-Liu equation derived from the reported equations for dye adsorption (47-49).

$$q_e = q_m \frac{K_L C_e}{1 + K_L C_e} + \left(q_{max} - q_{aq}\right) \frac{\left(K_g C_e\right)^{n_L}}{1 + \left(K_g C_e\right)^{n_L}} \quad (8)$$

Here K_L and K_g are the Langmuir and Liu adsorption constants, respectively. The q_m is the monolayer capacity and q_{ag} is the capacity as aggregation started on the surface. In general, aggregation initiates before monolayer is completed (i.e., $q_{ag} < q_m$). Therefore, the first term of Eq. 8 is valid until q_{ag} then the second term is added to q_{ag} value at higher concentrations.

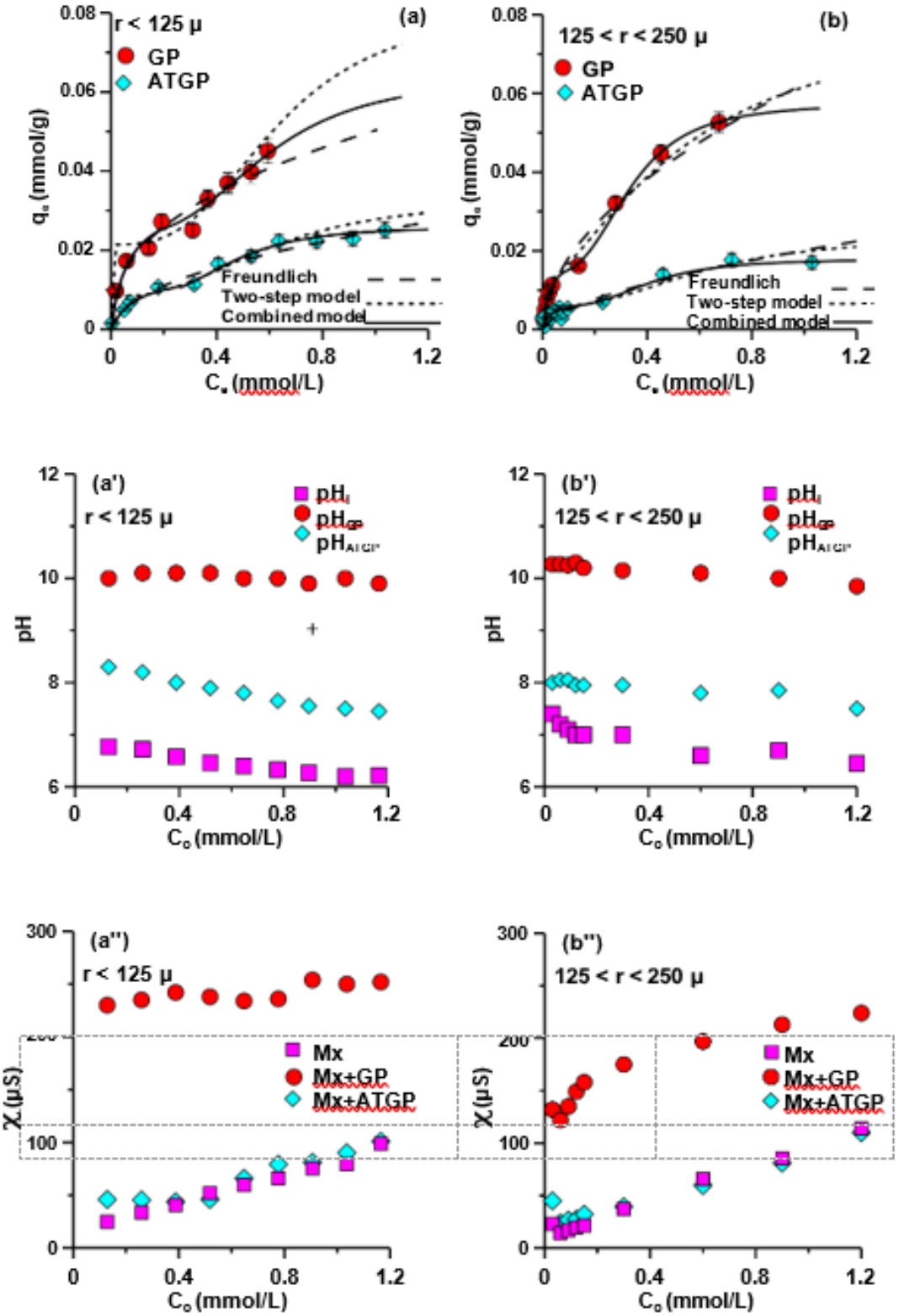

Figures 5: Adsorption isotherms of Mitoxantrone on the GP and ATGP on: a) r < 125 and b) 125 < r < 0.125 µm size adsorbents; The corresponding pH changes a' and b', and conductivity changes a'' and b'' in adsorption process depending on initial Mx concentration.

Table 2: The isotherm parameters for combined and two-step adsorption models for Mx adsorption on the glass powder.

Model	Adsorbent	r μm	q_m mmol/g	q_{ag} mmol/g	q_{max} mmol/g	n_L	K_L L/mmol	K_G L/mmol	σ mmol/g
Combined	GP	r < 125	00.34	0.024	0.064	2.7	15.00	1.70	0.002
		125 < r < 250	0.019	0.018	0.057	3.2	40.00	3.00	0.001
	ATGP	r < 125	0.015	0.008	0.026	3.3	10.00	2.20	0.001
		125 < r < 250	0.006	0.006	0.018	3.1	37.05	2.45	0.001
					q_{max} mmol/g	**n**		**K_2**	
Two-step	GP	r < 125			0.060	2.8		4.00	0.005
		125 < r < 250			0.070	6.0		2.50	0.009
	ATGP	r < 125			0.025	3.0		3.50	0.003
		125 < r < 250			0.018	3.1		3.50	0.003
					K_F mmol/g	**n_F**			
Freundlich	GP	r < 125			0.050	2.4			0.002
		125 < r < 250			0.063	1.9			0.003
	ATGP	r < 125			0.025	2.0			0.002
		125 < r < 250			0.020	1.7			0.017

The isotherm parameters used in calculations of theoretical curves are shown in Table 2. Slightly higher adsorption capacity was calculated for the larger size GP (0.070 mmol/g) than that of the smaller particles (0.060 mmol/g) due to high aggregation number predicted for drug molecules (n = 6). According to combined model, the capacities decrease with increasing particle size for both GP and ATGP at two-steps as expected. These values are more reasonable because of the same aggregation number predicted for Mx (~ 3) on both adsorbents. The lower capacities of ATGP confirm that surface sites on the GP available for chemical reactions are partly dissolved and porous structure is formed following acid treatment. Molecular dimensions Mx of 19.4 × 12.3 Å^2 is suitable for its diffusion into pores with 40 Å diameter. The Mx molecules are adsorbed on the pore walls by π- π interactions with anthracene unit. Hydrogen bonding interactions are also possible between – NH – moiety and oxide surface. The Mx adsorbed in the pores can be dissolved by body fluids in molecular form.

The isotherm data were also compared with commonly used Freundlich isotherm model given below:

$$q_e = K_F C_e^{1/n_F} \quad (9)$$

Here K_F and n_F are capacity and intensity factors, respectively.

Although Freundlich isotherm does not rely on a theoretical basis, it almost well fits adsorption data for natural adsorbents. The values of K_F presented in Table 2 are quite consistent with the capacities obtained from two step models. The n_F values higher than unity indicate favorable Mx adsorption on glass surfaces.

Adsorption capacities presented in Table 2 are 0.064, 0.060 and 0.050 mmol/g for r < 125 μm GP particles according to combined, two-step and Freundlich models, respectively. The same value of ~ 0.025 mmol/g is estimated for ATGP by all models.

Our values for GP of 0.064 mmol/g (33.1 mg/g) and ATGP of 0.026 mmol/g (13.5 mg/g) were compared some recent published data on drug adsorption onto special adsorbents, bioglass and solid wastes (Table 3). Mx adsorption on special adsorbents and drug adsorption on bioglass used as drug carriers changes in 371 – 97.4 and 126 – 2.53 mg/g, respectively. The drug adsorption capacities on solid wastes decreases from 20.6 to 1.43 mg/g used for water cleaning as low-cost adsorbents.

Initial pHs of the Mx solutions decrease from 7.40 to 6.45 as the concentration increased (Figures 5 a' and b'). The pH values of Mx solutions increase strongly up to ~ 10 after adsorption on the GP. As the GP is contacted with water pH values also attain to this value indicating dissolution of alkali and alkali earth oxides. The increment of the pH confirms that Mx chemically react with these cations on the surface. These results are also supported by the enhancement of the conductivities over 200 μS. On the other hand, the pH values slightly increase and change in 8.3 – 7.45 range at equilibrium. The small change in OH^- concentration ~ 10^{-6} mol/L is also reflected on the conductivity plot in Figures 5 a'' and b'' which remains nearly constant. This indicates that more stable glass surface is formed by acid treatment.

These results were also supported by the thermodynamic studies in the foll range owing section.

Table 3: Comparison of drug adsorption on several type adsorbents.

Adsorbent	Type	Drug	q_m mg/g	Ref
Zr-based (MOF) UiO-62	Special	Mitoxantrone	371	(7)
Zr-Based MOF UiO-62-NH_2		Mitoxantrone	208	
mSWCNT		Mitoxantrone	263	(8)
Bovine serum albumin-mSWCNT		Mitoxantrone	145	
MWCNT		Mitoxantrone	200	(9)
Biosynthesized Mn nanoparticles (MNPs)		Mitoxantrone	97.4	(10)
70SiO_2-26CaO-4 P_2O_5	Bioglass	Fluorouracil	126	(22)
Mesoporous bioglass		Simvastatin	122	(23)
80SiO_2–15CaO–5P_2O_5		Ciprofloxacin	31.0	(15)
70SiO_2–25CaO–5 P_2O_5		Doxycycline	29.0	(15)
Sol-gel bioglass 60S		Cisplatin	20.7	(24)
80SiO_2–15CaO–5 P_2O_5		Levofloxacin	2.53	(17)
Acid treated Fly ash	Low-cost	ciprofloxacin	20.6	(34)
Fly ash		ciprofloxacin	12.1	
Acidified red mud		ciprofloxacin	7.84	(33)
sugarcane bagasse		ciprofloxacin	2.61	(32)
sugarcane bagasse		diclofenac	1.81	
sugarcane bagasse		ibuprofen	1.62	
sugarcane bagasse		sulfamethoxazole	1.43	
Glass powder		Mitoxantrone	33.1	This work
Acid treated glass powder		Mitoxantrone	13.5	This work

3.4. Thermodynamics of Mx adsorption on the GP and ATGP

Distribution coefficient (K_D) is the ratio of adsorbate in adsorbent and solution. Its dimensionless form given below can be reasonably used for calculation of thermodynamic functions.

$$K_D = \frac{(C_o - C_e)}{C_e}\frac{m_s}{m_a} \quad (10)$$

where m_s is the solution mass.

The entropy ΔS^0 and enthalpy ΔH^0 changes for Mx adsorption were estimated from the intercept and slope of the straight-lines in Figure 6 drawn according to Van't Hoff equation.

$$lnK_D = \frac{\Delta S^0}{R}\frac{\Delta H^0}{RT} \quad (11)$$

The free energy change ($\Delta G°$) is also calculated from the Gibbs-Helmholtz equation.

$$\Delta G^0 = \Delta H^0 - T\Delta S^0 \quad (12)$$

The thermodynamic parameters for Mx adsorption evaluated from the distribution coefficients in 0.1 mM Mx solution in 298 – 350 K temperature range were presented in Table 4. The exothermic nature of Mx adsorption on the GP ($\Delta H < 0$) indicates that chemical bonds are formed between the glass surface and Mx molecules while the endothermic process on the ATGP ($\Delta H > 0$) is an indication of physical adsorption in the pores. The driving force of pore diffusion process is the positive entropy change which can provide controlled release of the drug molecules.

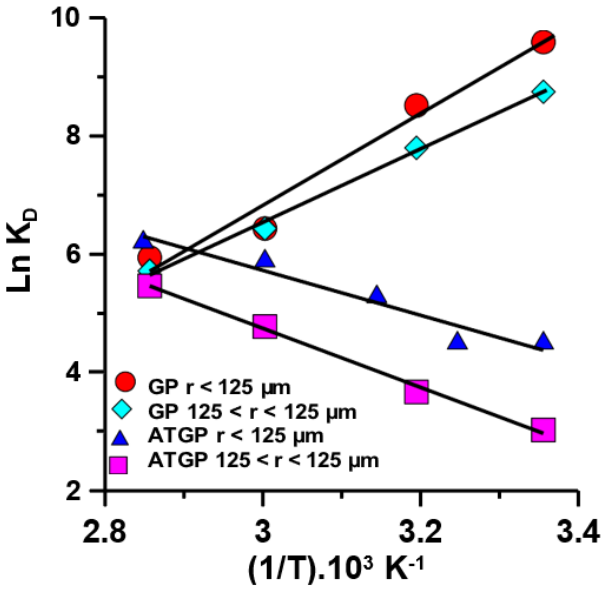

Figure 6: Van't Hoff plot for thermodynamic calculations of Mitoxantrone adsorption on the GP and ATGP.

Table 4: Thermodynamic parameters for Mx adsorption on the GP and ATGP.

	R µm	T K	dH kJ/mol	dS J/mol K	dG kJ/mol	R^2
GP	r < 125	298	-64.56	-0.137	-23.71	0.932
		313			-22.11	
		333			-17.78	
		350			-17.26	
GP	125 < r < 250	298	-51.59	-0.101	-21.63	0.990
		313			-20.25	
		333			-17.78	
		350			-16.60	
ATGP	r < 125	298	31.51	0.142	-11.11	0.939
		308			-11.48	
		318			-13.93	
		333			-16.25	
		351			-18.07	
ATGP	125 < r < 250	298	41.49	0.164	-7.48	0.996
		313			-9.53	
		333			-13.19	
		350			-15.87	

4. CONCLUSION

Acid treatment of the glass powder results in stabile porous surface which allows slow drug adsorption in the pores. The time dependency of Mx adsorption on the ATGP with different particle size was modeled by using the pseudo-first order, two-first order and homogeneous surface diffusion models. The two-first order model predicts the fast initial surface reaction followed by a slow pore diffusion which can provide controlled drug release in long term. Two-step adsorption isotherms are observed for Mx adsorption on both GP and ATGP powder. Adsorbed quantity of Mx decreased with increasing particle radius according to combined model derived from Langmuir and Liu equations. The equilibrium data fit better the combined model rather than two-step isotherm model. The second step corresponds to formation of drug aggregates in concentrated solutions. Although the GP has higher adsorption capacity than ATGP it is not suitable for drug release due to ultra-fast chemical adsorption on the surface. However, it can be used as environmentally friendly adsorbent for drug-removal in water cleaning, but ATGP is a promising adsorbent as drug-carrier.

5. REFERENCES

1. Badshah SL, Malik T, Ahmad N, Khan K, Ullah A, Ibrahim M. Mitoxantrones for Cancer Treatment and there Side Effects. JSM Clin Pharm.

2017;3(1):1011. Available from: <URL>.

2. Bernd H, De Kerviler E, Gaillard S, Bonnemain B. Safety and tolerability of ultrasmall superparamagnetic iron oxide contrast agent. Invest Radiol. 2009 Jun;44(6):336–42. Available from: <URL>.

3. Janko C, Dürr S, Munoz L, Lyer S, Chaurio R, Tietze R, et al. Magnetic drug targeting reduces the chemotherapeutic burden on circulating leukocytes. Int J Mol Sci. 2013 Apr 2;14(4):7341–55. Available from: <URL>.

4. Hornung A, Poettler M, Friedrich R, Zaloga J, Unterweger H, Lyer S, et al. Treatment efficiency of free and nanoparticle-loaded mitoxantrone for magnetic drug targeting in multicellular tumor spheroids. Molecules. 2015 Sep 30;20(10):18016–30. Available from: <URL>.

5. Zhu Y, Shi J, Shen W, Chen H, Dong X, Ruan M. Preparation of novel hollow mesoporous silica spheres and their sustained-release property. Nanotechnology. 2005 Nov 1;16(11):2633–8. Available from: <URL>.

6. Heleg-Shabtai V, Aizen R, Sharon E, Sohn YS, Trifonov A, Enkin N, et al. Gossypol-capped mitoxantrone-loaded mesoporous SiO_2 NPs for the cooperative controlled release of two anti-cancer drugs. ACS Appl Mater Interfaces. 2016 Jun 15;8(23):14414–22. Available from: <URL>.

7. Singhal M, Riches-Suman K, Pors K, Addicoat MA, Ruiz A, Nayak S, et al. Encapsulation and delivery of mitoxantrone using zirconium-based metal–organic frameworks (MOFs) and their cytotoxic potential in breast cancer cells. Appl Sci. 2024 Feb 26;14(5):1902. Available from: <URL>.

8. Aydın B, Bozoğlu S, Karatepe N, Güner FS. Synthesis of bovine serum albumin-coated magnetic single-walled carbon nanotubes as a delivery system for mitoxantrone. ACS Omega. 2025 Jan 14;10(1):102–13. Available from: <URL>.

9. Risi G, Bloise N, Merli D, Icaro-Cornaglia A, Profumo A, Fagnoni M, et al. Invitro study of multiwall carbon nanotubes (MWCNTs) with adsorbed mitoxantrone (MTO) as a drug delivery system to treat breast cancer. RSC Adv. 2014;4(36):18683–93. Available from: <URL>.

10. He F, Cai W, Lin J, Yu B, Owens G, Chen Z. Reducing the impact of antibiotics in wastewaters: Increased removal of mitoxantrone from wastewater by biosynthesized manganese nanoparticles. J Clean Prod. 2021 Apr;293:126207. Available from: <URL>.

11. Huang M, Chen S, Huang J, Gerald RE, Woelk K. NMR studies of materials loaded into porous-wall hollow glass microspheres. Mater Sci Eng C. 2020 Nov;116:111177. Available from: <URL>.

12. Moosavi SS, Alizadeh P. Effect of acid leaching time on pore diameter and volume of porous hollow glass microspheres. Mater Lett. 2016 Mar;167:98–101. Available from: <URL>.

13. Li S, Nguyen L, Xiong H, Wang M, Hu TCC, She JX, et al. Porous-wall hollow glass microspheres as novel potential nanocarriers for biomedical applications. Nanomedicine Nanotechnology, Biol Med. 2010 Feb;6(1):127–36. Available from: <URL>.

14. Galbreath S, Krueger B, Frazier T, Goswami T. Effectiveness of mesoporous bioglass in drug delivery. J Pharm Biopharm Res. 2022;4(1):271–82. Available from: <URL>.

15. Gómez-Cerezo N, Lozano D, Salinas AJ, Vallet-Regí M. Mesoporous bioactive glasses: A powerful tool in tissue engineering and drug delivery. Adv Healthc Mater. 2026 Jan 11;15(2):e02201. Available from: <URL>.

16. Wang Y, Li F, Xin J, Xu J, Yu G, Shi Q. Mesoporous drug delivery system: From physical properties of drug in solid state to controlled release. Molecules. 2023 Apr 12;28(8):3406. Available from: <URL>.

17. Elnahas OS, Osama R, Abdel-Haleem KM, El-Nabarawi MA, Teaima MH, El-Sadek HM, et al. Integration of levofloxacin-loaded spanlastics and prednisolone into a buccal mucoadhesive sponge for combating severe pneumonia: In-vitro/ex-vivo assessment, qRT-PCR analysis, and quantification of the HMGB-1/NF-κB signaling pathway. J Drug Deliv Sci Technol. 2024 Oct;100:106019. Available from: <URL>.

18. Parhad TH, Robel FN, Bahadur NM, Tabassum S, Dey SS, Ali MF, et al. Preparation of bio-glass and bio-ceramic utilizing sol-gel method and fabrication of bio-scaffolds for drug loading and releasing application. Ceram Int. 2025 Sep;51(21):32771–83. Available from: <URL>.

19. Skwira A, Szewczyk A, Barros J, Laranjeira M, Monteiro FJ, Sądej R, et al. Biocompatible antibiotic-loaded mesoporous silica/bioglass/collagen-based scaffolds as bone drug delivery systems. Int J Pharm. 2023 Oct;645:123408. Available from: <URL>.

20. El Baakili S, El Mabrouk K, Bricha M. Acellular bioactivity and drug delivery of new strontium doped bioactive glasses prepared through a hydrothermal process. RSC Adv. 2022;12(24):15361–72. Available from: <URL>.

21. Liu QR, Dai YC, Ji LJ, Gong MD, Li X, Fang J, et al. Preparation of ropivacaine-loaded mesoporous bioactive glass microspheres and evaluation of their efficacy for sciatic nerve block. J Drug Deliv Sci Technol. 2020 Aug;58:101810. Available from: <URL>.

22. El-Kady AM, Farag MM. Bioactive glass nanoparticles as a new delivery system for

sustained 5-fluorouracil release: Characterization and evaluation of drug release mechanism. Yang P, editor. J Nanomater. 2015 Jan 2;2015(1):839207. Available from: <URL>.

23. Yao H, Luo J, Deng Y, Li Z, Wei J. Alginate-modified mesoporous bioactive glass and its drug delivery, bioactivity, and osteogenic properties. Front Bioeng Biotechnol. 2022 Oct 5;10:994925. Available from: <URL>.

24. Kusyak AP, Petranovska AL, Dubok VA, Chornyy VS, Bur'yanov OA, Korniichuk NM, et al. Adsorption immobilization of chemotherapeutic drug cisplatin on the surface of sol-gel bioglass 60S. Funct Mater. 2021 Mar 22;28(1):97–105. Available from: <URL>.

25. Tabia Z, El Mabrouk K, Bricha M, Nouneh K. Mesoporous bioactive glass nanoparticles doped with magnesium: Drug delivery and acellular *in vitro* bioactivity. RSC Adv. 2019;9(22):12232–46. Available from: <URL>.

26. Bonnet C, Bouquillon A, Turrell S, Deram V, Mille B, Salomon J, et al. Alteration of lead silicate glasses due to leaching in heated acid solutions. J Non Cryst Solids. 2003 Aug;323(1–3):214–20. Available from: <URL>.

27. Angeli F, Gaillard M, Jollivet P, Charpentier T. Influence of glass composition and alteration solution on leached silicate glass structure: A solid-state NMR investigation. Geochim Cosmochim Acta. 2006 May;70(10):2577–90. Available from: <URL>.

28. Toquer G, Delchet C, Nemec M, Grandjean A. Effect of leaching concentration and time on the morphology of pores in porous glasses. J Non Cryst Solids. 2011 Mar;357(6):1552–7. Available from: <URL>.

29. De Bardi M, Wiesinger R, Schreiner M. Leaching studies of potash–lime–silica glass with medieval composition by IRRAS. J Non Cryst Solids. 2013 Jan;360:57–63. Available from: <URL>.

30. Gomes Fernandes R, Al-Mukadam R, Bornhöft H, Reinsch S, Müller R, Selle S, et al. Viscous sintering of acid leached glass powders. Glas Eur. 2023 Nov 23;1:37–53. Available from: <URL>.

31. Zhao J, Liu S. Different acid-leaching processes of HCl, H_2SO_4 and H_3PO_4 leading to the formation of porous glass-ceramic photocatalysts with different crystalline phases via a unified mechanism. Ceram Int. 2024 Jan;50(1):1725–31. Available from: <URL>.

32. Peñafiel ME, Flores D. Competitive adsorption of drugs from a multi-component mixture on sugarcane bagasse. Water. 2023 Jun 3;15(11):2127. Available from: <URL>.

33. Shi J, Wang W, Li Z, Shi Y. Ciprofloxacin Removal via Acid-Modified Red Mud: Optimizing the Process, Analyzing the Adsorption Features, and Exploring the Underlying Mechanism. Molecules. 2024 Jun 20;29(12):2928. Available from: <URL>.

34. Wang J, Li X, Lan Y, Wang H, Ma X, Wang H, et al. Study on the adsorption mechanism of ciprofloxacin in wastewater by modified fly ash under the coexistence of copper. J Environ Chem Eng. 2024 Dec;12(6):114336. Available from: <URL>.

35. Atun G, Hisarlı G, Tunçay M. Adsorption of safranine-O on hydrophilic and hydrophobic glass surfaces. Colloids Surfaces A Physicochem Eng Asp. 1998 Dec;143(1):27–33. Available from: <URL>.

36. Atun G, Hisarli G. Adsorption of carminic acid, a dye onto glass powder. Chem Eng J. 2003 Sep;95(1–3):241–9. Available from: <URL>.

37. Sklute EC, Jensen HB, Rogers AD, Reeder RJ. Morphological, structural, and spectral characteristics of amorphous iron sulfates. J Geophys Res Planets. 2015 Apr 30;120(4):809–30. Available from: <URL>.

38. Runowski M, Stopikowska N, Lis S. UV-Vis-NIR absorption spectra of lanthanide oxides and fluorides. Dalt Trans. 2020;49(7):2129–37. Available from: <URL>.

39. Jantzen CM, Trivelpiece CL, Crawford CL, Pareizs JM, Pickett JB. Accelerated leach testing of GLASS (ALTGLASS): I. Informatics approach to high level waste glass gel formation and aging. Int J Appl Glas Sci. 2017 Mar 18;8(1):69–83. Available from: <URL>.

40. Crowley JK, Williams DE, Hammarstrom JM, Piatak N, Chou IM, Mars JC. Spectral reflectance properties (0.4–2.5 μm) of secondary Fe-oxide, Fe-hydroxide, and Fe-sulphate-hydrate minerals associated with sulphide-bearing mine wastes. Geochemistry Explor Environ Anal. 2003 Aug 6;3(3):219–28. Available from: <URL>.

41. Viscarra Rossel RA, McGlynn RN, McBratney AB. Determining the composition of mineral-organic mixes using UV–vis–NIR diffuse reflectance spectroscopy. Geoderma. 2006 Dec;137(1–2):70–82. Available from: <URL>.

42. Revellame ED, Fortela DL, Sharp W, Hernandez R, Zappi ME. Adsorption kinetic modeling using pseudo-first order and pseudo-second order rate laws: A review. Clean Eng Technol. 2020 Dec;1:100032. Available from: <URL>.

43. Inglezakis VJ, Grigoropoulou HP. Applicability of simplified models for the estimation of ion exchange diffusion coefficients in zeolites. J Colloid Interface Sci. 2001 Feb;234(2):434–41. Available from: <URL>.

44. Ortaboy S, Atun G. Kinetics and equilibrium modeling of uranium(VI) sorption by bituminous shale from aqueous solution. Ann Nucl Energy. 2014 Nov;73:345–54. Available from: <URL>.

45. Labiano A, Dai M, Taylor D, Young WS, Epps TH, Rege K, et al. Slow release kinetics of mitoxantrone from ordered mesoporous carbon films. Microporous Mesoporous Mater. 2012 Sep;160:143–50. Available from: <URL>.

46. Kalam S, Abu-Khamsin SA, Kamal MS, Patil S. Surfactant Adsorption Isotherms: A Review. ACS Omega. 2021 Dec 7;6(48):32342–8. Available from: <URL>.

47. Cantürk Talman RY, Kurtoğlu AE, Atun G. Surface modification of fly ash by sodium dodecyl sulfate for enhancement of cetyl pyridinium chloride adsorption. J Mol Liq. 2025 Nov;438:128733. Available from: <URL>.

48. Atun G, Ayar N, Kurtoğlu AE, Ortaboy S. A comparison of sorptive removal of anthraquinone and azo dyes using fly ash from single and binary solutions. J Hazard Mater. 2019 Jun;371:94–107. Available from: <URL>.

49. Kurtoğlu AE, Ortaboy Sezer S, Acar ET, Tüzün E, Atun G. Design of two-step isotherms for enhancement sorption efficiency of C-type fly ash for acid and basic dyes and prediction of their chemical reactivities using DFT calculations. Water, Air, Soil Pollut. 2025 Dec 4;236(14):908. Available from: <URL>.